ACS Photonics

Article

pubs.acs.org/journal/apchd5

Second-Harmonic Enhancement with Mie Resonances in Perovskite Nanoparticles

Flavia Timpu,*,† Anton Sergeyev,† Nicholas R. Hendricks,† and Rachel Grange†

†Optical Nanomaterial Group, Institute for Quantum Electronics, Department of Physics, ETH Zurich, Auguste Piccard Hof 1, 8093 Zurich, Switzerland

Supporting Information

ABSTRACT: Second-harmonic generation (SHG) in nanostructures gives rise to many applications such as lab-on-a-chip and imaging by frequency doubling. However, the SHG signal decreases with volume, and the conversion efficiency is limited. Thus, means to enhance nonlinear signals at the nanoscale are needed. For instance, while plasmonic nanostructures offer a high enhancement due to the strong confinement of the electromagnetic field, they have high losses and the fabrication methods are difficult. In this work, we propose to enhance the SHG by using the intrinsic scattering properties of an all-dielectric perovskite nanostructure. We demonstrate the Mie scattering resonances of individual barium titanate ($BaTiO_3$) nanoparticles with diameters between 200 and 250 nm. We distinguish contributions of the magnetic dipole and magnetic quadrupole. Then, we use the Mie resonances to achieve an SHG enhancement of 4 orders of magnitude within the same nanoparticle. Our results suggest that a strong increase of the SHG signal can be obtained without using plasmonic or hybrid nanostructures. We show a straightforward way of enhancing low optical signals within a single material, which will facilitate the study of other nonlinear phenomena at the nanoscale.

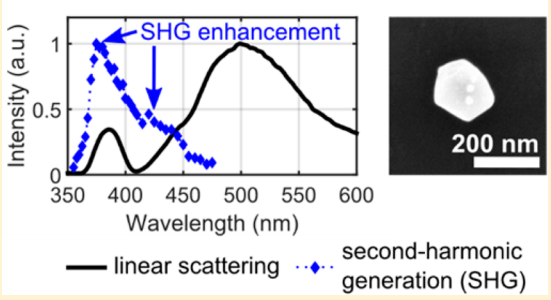

KEYWORDS: *nonlinear optics, perovskite, nanoparticle, second-harmonic generation, Mie scattering*

Dielectric-based nanomaterials have gained significant interest for their applications as metamaterials[1] and nanophotonics devices.[2] Their advantages over the well-established plasmonic nanodevices[3] are the reduced losses in the visible range and their multiple optical resonances. Therefore, the dielectric nanomaterials are potential building blocks for tailoring separate electric and magnetic responses. As a typical all-dielectric material, silicon nanoparticles exhibit strong Mie-type[4] magnetic and electric resonances in the visible range due to the high refractive index.[5,6] As a result, silicon nanoantennas[7] and single nanocylinders for metasurfaces[8,9] have been recently demonstrated. By tuning the electric and magnetic response of these nanostructures, highly efficient and flexible light manipulation can be achieved at the nanoscale. The tailoring of the optical properties is possible because the scattering cross-section strongly depends on the wavelength,[4] the shape,[5] and the optical properties of the dielectric nanostructures.[10]

Besides linear optical effects, nonlinear optical effects such as second-harmonic generation (SHG) are also desirable in plasmonic and dielectric nanostructures. Since SHG requires a break of symmetry, it can occur only in the bulk of non-centrosymmetric materials or at a material interface.[11] Substantial research effort has been invested into increasing the conversion efficiency of the incident beam to the SHG signal. Despite their symmetric crystal structure, pure metallic nanostructures have been shown to emit strong nonlinear signals[12] due to shape asymmetry,[13,14] surface contributions,[14] or tip enhancement.[15] However, these nanostructures have high losses in the visible range and small volumes and their asymmetric shapes require complex fabrication methods. A strong SHG enhancement can also be achieved in hybrid structures. We have demonstrated a 2 orders of magnitude SHG enhancement in hybrid barium titanate ($BaTiO_3$) nanoparticles[16] and potassium niobate ($KNbO_3$) nanowires[17] with gold shells. SHG enhancement has also been shown in lithium niobate ($LiNbO_3$) disks surrounded by gold nanorings.[18] Besides, an SHG enhancement has been achieved by placing a dielectric material between metallic nanoantennas.[19−21] While hybrid metallic−dielectric nanostructures offer a significant enhancement of the SHG conversion efficiency, they also inherit the drawbacks of pure plasmonic nanostructures. Furthermore, the core−shell thickness ratio is a critical parameter.[16] Therefore, eliminating the metallic structure would improve the nonlinear response of nanostructures. One method to enhance the nonlinear response of bare dielectric nanoparticles is by taking advantage of their intrinsic scattering resonances. Recently, semiconductor metasurfaces fabricated by top-down approaches were used to demonstrate the nonlinear effects at the linear resonances. For instance, the Fano resonance has been successfully used to enhance the

Received: August 4, 2016
Published: December 16, 2016

 © 2016 American Chemical Society

DOI: 10.1021/acsphotonics.6b00570
ACS Photonics 2017, 4, 76−84

third-order nonlinearity of a centrosymmetric silicon metasurface.[22] Third-harmonic generation enhancement originating from the Mie resonance was shown for arrays of silicon nanodisks,[23] and the enhancement of SHG at the Mie resonance was measured on metasurfaces of gallium arsenide (GaAs) nanodisks.[24] Furthermore, the size dependence of the SHG intensity from aluminum gallium arsenide (AlGaAs) nanopillars was shown to depend on the confinement of the electromagnetic field inside the nanopillars.[25] Semiconductors such as silicon, GaAs, and AlGaAs show significant absorption in the visible spectrum due to their band gap.[26,27] Moreover, they have a low laser damage threshold[24] and poor compatibility for bioapplications.[28] Finally, the nonlinear signal originating from metasurfaces has higher intensity, as it originates from a collection of nanostructures.

Here, we propose to take advantage of the Mie scattering resonances of the nanomaterial itself to enhance the SHG signal from an individual $BaTiO_3$ nanoparticle. For this purpose, we use single nanoparticles of $BaTiO_3$ material, which is transparent in visible and infrared ranges[29] and is proved to be biocompatible.[30] Moreover, $BaTiO_3$ belongs to the group of perovskite materials and has a non-centrosymmetric crystal structure. $BaTiO_3$ nanoparticles show a strong bulk SHG ability even at the nanoscale size.[31] Due to the large refractive index, $BaTiO_3$ nanoparticles are expected to have several resonances in the linear scattering cross-section.

In this work, we study the linear and the nonlinear properties of individual $BaTiO_3$ nanoparticles in a wide wavelength range. We demonstrate that an individual $BaTiO_3$ nanoparticle uses its own intrinsic optical resonances to enhance the emitted SHG. At the plasmonic resonances, the enhancement of the nonlinear signal is caused by the confinement of the electromagnetic field around the metallic surface. Contrary to plasmonics, at the Mie resonance the highest confinement of the electromagnetic field occurs inside the dielectric nanostructure. Since the SHG of $BaTiO_3$ nanoparticles originates from the bulk, this confinement increases the conversion efficiency to SHG, resulting in an enhancement of the nonlinear signal. Therefore, without using metals or hybrid nanostructures, we achieve a significant SHG enhancement.

We start by measuring the linear scattering spectrum of single $BaTiO_3$ nanoparticles. We show that the nanoparticles have two Mie resonances that are dominantly caused by the magnetic dipole and magnetic quadrupole contributions. Furthermore, we measure a strong SHG signal from individual nanoparticles. We prove that the SHG signal correlates with the linear spectrum of the single nanoparticle. Finally, as the linear spectrum influences the nonlinear spectrum directly, we perform finite element methods (FEM) simulations of the scattering cross-section of individual nanoparticles by taking the experimental conditions into account. Therefore, we determine the influence of the particle shape, of the substrate, and of the incidence angle on the linear properties of the $BaTiO_3$ nanoparticles. The FEM simulation reveals the origin of the blue-shift of the peaks in the linear scattering spectra compared to the expected peaks positions according to the Mie theory.

■ RESULTS AND DISCUSSION

Backscattering of Individual $BaTiO_3$ Nanoparticles. $BaTiO_3$ powders of nanoparticles are synthesized by a hydrothermal process.[32] X-ray diffraction (XRD) measurements reveal that the $BaTiO_3$ nanoparticles have a 90% tetragonal crystallographic structure (Supporting Information Figure 1S). The $BaTiO_3$ nanoparticles are then suspended in ethanol with a low concentration (0.05 μg/mL) and spin coated on a glass substrate. The glass substrate is initially coated with an indium tin oxide (ITO) layer and prepatterned with coordinates to facilitate the localization of the nanoparticles for the optical and the scanning electron microscopy (SEM) measurements.

First, we determine the position and the number of the Mie resonances in the linear scattering spectrum. To this end, we measure the linear scattering spectra of several single $BaTiO_3$ nanoparticles of similar sizes (200 to 250 nm) in a dark field spectroscopy setup (Figure 1). The nanoparticles are

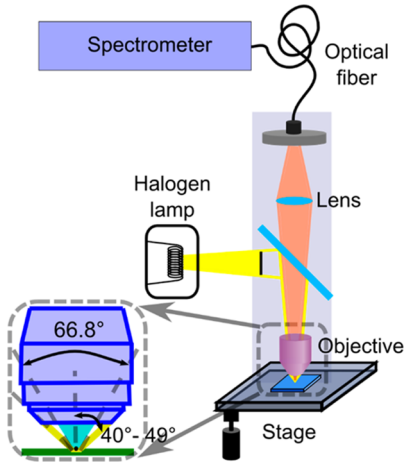

Figure 1. Dark field spectroscopy setup for linear scattering measurements with the optical fiber acting as a pinhole. Inset: Schematics of the 50× objective: The incident light reaches the nanoparticle under an incidence angle of 40−49°. The objective collects the signal within 33.4° of its optical axis.

illuminated by a halogen lamp through a 50× dark field objective. The backscattering of each nanoparticle is collected with the same objective and measured with an imaging spectrometer through a multimode fiber. The fiber acts as a pinhole and collects only the signal around an individual nanoparticle. The diameter of the collection area in this setup configuration is 5 μm. The nanoparticle is positioned within the collection area of the optical fiber using the manual stage. The signal is corrected for background contributions and wavelength dependence of the halogen lamp spectrum. Examples of single-particle scattering spectra and the corresponding SEM images are shown in Figure 2.

The selected nanoparticles have similar diameters of about 200−250 nm. Due to the fabrication method (hydrothermal growth), the nanoparticles have irregular ellipsoidal shapes. Clear facets are visible in the SEM micrographs, confirming the crystalline structure. The linear scattering spectra (Figure 2a−g) show two distinct peaks. In order to understand the origin of these peaks, we calculate the scattering cross-section of a 200 nm spherical $BaTiO_3$ nanoparticle in a homogeneous medium (air). The size of the nanoparticles is comparable to the wavelength of the incident light. Therefore, the linear response does not resemble the spectrum of a Rayleigh scatterer. Due to the size of the nanoparticle, the electromagnetic field inside the nanoparticle is not constant and multiple modes are generated. These modes are described by the Mie theory[4] as individual multipole contributions. In the calculation, we use the bulk refractive index values of $BaTiO_3$.[33] Figure 2h displays the

DOI: 10.1021/acsphotonics.6b00570
ACS Photonics 2017, 4, 76−84

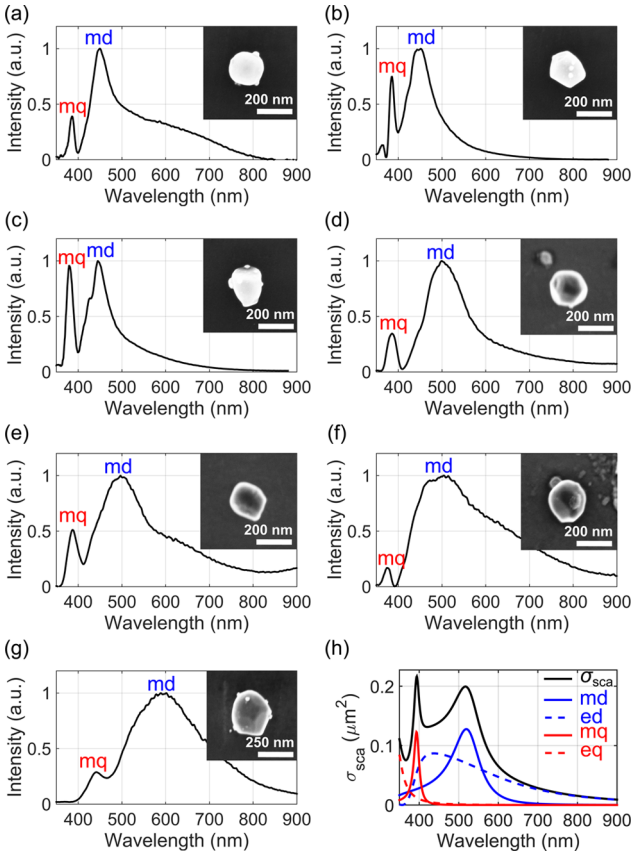

Figure 2. Linear scattering spectra of individual $BaTiO_3$ nanoparticles. (a−g) Spectra of the backscattered light from single $BaTiO_3$ nanoparticles measured in the dark field spectroscopy setup (Figure 1). The data were normalized to the maximum value of the backscattering intensity. The insets show SEM micrographs of the measured nanoparticles. The origin of the peaks is also depicted (*md*, magnetic dipole; *mq*, magnetic quadrupole). (h) Analytical calculation of the scattering cross-section (black line) of a $BaTiO_3$ nanoparticle with a diameter of 200 nm. The individual multipole contributions are depicted (*md*, magnetic dipole, blue line; *ed*, electric dipole, blue dashed line; *mq*, magnetic quadrupole, red line; *eq*, electric quadrupole, red dashed line).

calculated Mie scattering spectrum and the individual multipole contributions to the spectrum. Figure 2S (Supporting Information) shows the characteristic distribution of the modulus (norm) of the total electric and total magnetic fields inside the nanoparticles at the resonances in the Mie spectrum. The magnetic dipole (*md*) peak at 525 nm is clearly visible in the scattering spectrum (Figure 2h). The magnetic dipole is characterized by a radial electric field and a transversal magnetic field inside the nanoparticle (Supporting Information Figure 2Sd). For comparison, we calculate the linear scattering spectrum of a Si particle of identical size. The scattering cross-section of a similar Si nanoparticle of 200 nm diameter has well separated *md* and electric dipole (*ed*) peaks at 606 and 774 nm, respectively (Supporting Information Figure 3S). Contrary to the Si nanoparticle, the *ed*-peak at 420 nm of the $BaTiO_3$ nanoparticle (Figure 2h) is very close to the magnetic quadrupole (*mq*) peak at 400 nm and has a slowly decreasing tail that overlaps with the *md* contribution. This is due to the lower refractive index of $BaTiO_3$ (2.61 at 420 nm) compared to Si (3.93 at 606 nm). The optical path in a Si nanoparticle of identical size is longer than in the $BaTiO_3$ nanoparticle, and the separation of the multipole contributions is therefore larger than in $BaTiO_3$. As a consequence, the *ed* does not appear as an individual peak in the single particle spectrum of $BaTiO_3$, but only broadens the *md*- and *mq*-peaks. As a result, the two peaks in the measured spectra (Figure 2a−g) can be attributed to the *mq* and *md* contributions, respectively.

Several differences between the measured and calculated scattering spectra are observed. The positions of the two peaks in the measured linear scattering spectra (Figure 2a−f: the *mq*-peak around 380 nm and the *md*-peak around 450−500 nm) are in the same wavelength range as the calculated values (Figure 2h: *mq*-peak at 400 nm, *md*-peak at 520 nm), but a clear blue-shift of the experimental values is observed. Furthermore, the ratio between the intensities of the two measured peaks shows discrepancies with respect to the calculated spectrum. The *mq*-peak is usually less intense than the *md*-peak in the experimental data, whereas the *mq*-peak is more intense in the calculated spectra (Figure 2h). Finally, the *md*-peaks of the scattering spectra depicted in Figure 2e−g have a more pronounced tail in the 600−800 nm range. This signal is probably caused by contamination from organic material around the nanoparticles.

The size and the shape of the nanoparticle play a crucial role in their interaction with the electromagnetic field. The shape of the particle affects not only its linear properties but also its nonlinear properties.[34] The medium surrounding the nanoparticle, in particular the dielectric substrate, influences the emission pattern of the nanostructure.[35] A thorough understanding of the influence of these factors on scattering cross-section of $BaTiO_3$ nanoparticles is therefore required. After presenting the SHG spectra measurements, we perform and discuss several FEM models that take the shape of the nanoparticles and the substrate into account.

Wavelength-Dependent SHG Measurements of Individual $BaTiO_3$ Nanoparticles. The SHG of several single $BaTiO_3$ nanoparticles is measured for a broad wavelength range in two different setups. The first measurements are conducted in a commercial scanning multiphoton inverted microscope with a femtosecond (fs) Ti:sapphire laser source. Then, the measurements from the commercial setup are checked by a measurement in a home-built setup. In the commercial setup (Supporting Information Figure 4S), the incident laser beam is focused on the nanoparticle and scanned over an area of 144 μm^2 around the nanoparticle. The SHG is collected by the same objective and measured directly by external hybrid detectors. The reflected incident laser beam is filtered from the SHG signal with short-pass filters. The data are normalized to the laser power and the transmission of the optical components. The measurement is also conducted for a 144 μm^2 area without the $BaTiO_3$ nanoparticles in order to measure the background. The detected background is within the value of the intensity fluctuations of the detector. The SHG is measured for incident beam wavelengths between 710 and 950 nm with a step of 5 nm, giving an SHG signal in the range from 355 to 425 nm.

The measurement of the SHG signal from the single nanoparticles in the scanning system is fast and robust and demonstrates the response of the nanoparticles in a possible biological application setup. However, this system does not allow the spectrum of the emitted signal to be checked precisely for each laser wavelength. The use of a short-pass filter does not exclude the presence of photoluminescence. Furthermore, due to patent reasons, the transmissions of some components in the

DOI: 10.1021/acsphotonics.6b00570
ACS Photonics 2017, 4, 76−84

commercial system is unknown. To demonstrate that the spectra obtained in the commercial system are indeed SHG, further SHG measurements on one of the nanoparticles are performed in a home-built reflection microscope shown in Figure 3. In this setup, the nanoparticle is irradiated with a similar Ti:sapphire fs laser, as in the commercial setup. The incident laser beam is focused on the nanoparticle through a 50× objective. The backscattered signal is collected by the same objective and measured with an electron multiplying charge-coupled device (EMCCD) camera and an imaging spectrometer. The signal from the nanoparticle is filtered by color filters and a dichroic mirror to cut the pump wavelength. The image from the EMCCD camera is used to visualize the SHG signal and ensure the correct alignment between the incident laser beam spot and the nanoparticle. The intensity of the SHG signal is measured with the imaging spectrometer, which allows a clear separation of the SHG signal. The raw signal from the spectrometer is normalized to the incident laser power and the transmission of the setup. In this setup, each optical component is accurately calibrated for every wavelength of the incident laser beam and the absolute intensity of the SHG measurements can be measured.[36] Furthermore, the spectrometer allows a precise characterization of the signal emitted by the nanoparticle and the separation of the SHG signal from the incident laser beam (Supporting Information Figure 5S).

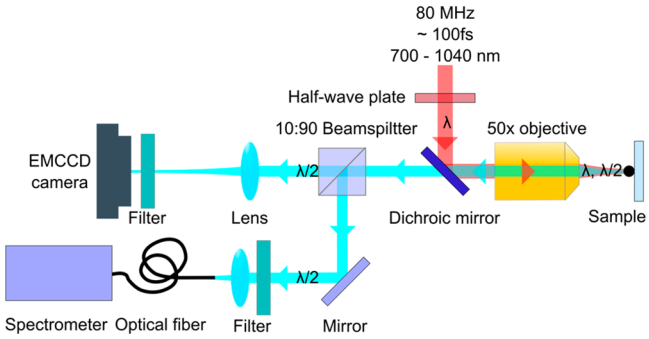

Figure 3. Home-built setup for detection of the wavelength-dependent SHG signal of a single nanoparticle. The femtosecond (fs) incident laser beam is focused on the sample by a 50× objective. The backscattered signal is collected and sent to an EMCCD camera and an imaging spectrometer. The reflected incident laser beam is filtered by color filters and a dichroic mirror. The SHG is measured for incident beam wavelengths between 700 and 1040 nm.

The SHG spectra and the corresponding scattering linear spectra are depicted in Figure 4a−d. The SHG signal depends strongly on the wavelength of the incident beam, and several peaks are observed. In Figure 4a−d, these peaks are highlighted by numbered green arrows, and their positions are summarized in Table 1. The first peak (numbered 1 in Figure 4a−d) occurs at the *mq*-peak. The third peak (numbered 3 in Figure 4a,b) is detected for the first and second nanoparticles (Figure 4a and b), but does not appear for the third nanoparticle (Figure 4c,d). This peak occurs in the proximity of the *md*-resonances. The second peak (numbered 2 in Figure 4a−d) appears between the *mq*- and the *md*-resonances. The second peak has the strongest SHG intensity for the first nanoparticle (Figure 4a), but has the aspect of a shoulder for the third particle (Figure 4c,d). Therefore, the measured SHG signal is clearly enhanced around the resonances of the linear backscattering spectrum for all the measured nanoparticles. The ratio between the highest and lowest SHG signal of the third nanoparticle is 17 (Figure 4c,d).

The SHG spectrum measured with the home-built setup is shown in Figure 4d. This measurement is in excellent agreement with the SHG spectrum measured from the same nanoparticle in the commercial setup (Figure 4c and d, respectively). In the home-built setup the same ratio of 17 between the highest and the lowest SHG signal is found. Therefore, the measurement in the homemade setup confirms that the signal detected from the nanoparticles in the commercial system is indeed SHG. No fluorescence or luminescence from the $BaTiO_3$ nanoparticle or the ITO conductive layer is detected by the spectrometer.

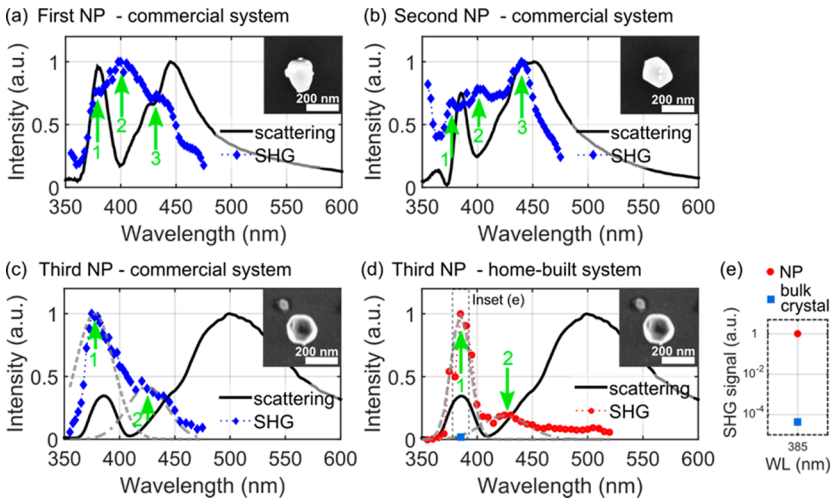

Figure 4. SHG spectra of individual $BaTiO_3$ nanoparticles (NP). The black continuous line represents the normalized backscattering linear spectrum of the nanoparticles. The blue diamond (a−c)/red dot (d) lines represent the normalized SHG signal values for the same nanoparticle. The gray dashed lines in (c) and (d) are Gaussian fits that serve for guiding the eye. The insets show the SEM micrographs of the measured $BaTiO_3$ nanoparticles. The numbered green arrows highlight the positions of the peaks in the SHG spectrum. The spectra (a)−(c) were measured with the commercial scanning multiphoton microscope. The spectrum in (d) was measured in the home-built setup (Figure 3). (e) Comparison between the SHG emitted by the third nanoparticle and by a bulk $BaTiO_3$ crystal at the resonant wavelength of 385 nm. The SHG from the bulk crystal was normalized to the SHG from the nanoparticle, and the results are shown on a logarithmic scale.

DOI: 10.1021/acsphotonics.6b00570
ACS Photonics 2017, 4, 76−84

Table 1. Measured Peak Positions in the Linear Scattering Spectrum and the SHG Spectrum

nanoparticle	spectrum	peak position		
		peak 1[c] magnetic quadrupole	peak 2[c] electric dipole	peak 3[c] magnetic dipole
1	linear[a]	381 nm		444 nm
	SHG[b]	380 nm	400 nm	432 nm
2	linear	385 nm		447 nm
	SHG	378 nm	400 nm	440 nm
3	linear	386 nm		500 nm
	SHG	375/385 nm	425/425 nm	

[a]Peak positions from the linear scattering spectrum (Figure 4a−d). [b]Peak position from the SHG spectrum (Figure 4a−d). [c]The peak numbers correspond to the numbered arrows in Figure 4a−d.

In previous works[22,24,25] the enhancement of the nonlinear signal from metasurfaces is calculated by comparing the patterned metasurface to the unpatterned original surface. This direct comparison is not possible in the case of single $BaTiO_3$ nanoparticles that were chemically synthesized. Indeed, SHG is highly dependent on the crystalline structure, and a consistent measurement of the enhancement can be made only by comparing a layer and a nanoparticle of $BaTiO_3$ with the same crystal structure and orientation. The fabrication methods of $BaTiO_3$ nanoparticles and layers are different, resulting in different crystalline orientations. Furthermore, $BaTiO_3$ layers with a thickness comparable to the diameter of the nanoparticles are not monocrystalline.[37,38] However, an estimated value of the SHG enhancement in the $BaTiO_3$ nanoparticle can be obtained by comparison with a bulk $BaTiO_3$ crystal. The SHG emitted by the bulk crystal is measured in the home-built setup (Figure 3) at the first resonance of the third nanoparticle (385 nm) (Figure 4d). The *c*-axis of the bulk crystal is parallel to the main face of the bulk crystal, and the polarization orientation is maximized to obtain the highest SHG signal (see the Supporting Information, Section 9, for a detailed description of the $BaTiO_3$ bulk crystal measurements). The results of the SHG signal from the bulk crystal and the nanoparticle at the same resonance wavelength (385 nm) are shown in Figure 4d (linear *y*-axis) and Figure 4e (log *y*-axis). The $BaTiO_3$ nanoparticle produces an enhancement of 8.9×10^4, more than 4 orders of magnitude compared to the bulk crystal (Figure 4e).

The origin of the SHG enhancement at the resonances in the linear spectrum can be referred to the distribution of the electromagnetic field inside the particle (Supporting Information Figure 2S). In the case of plasmonic nanostructures, the SHG signal is enhanced at the positions where the electromagnetic field is confined. Similarly, at the Mie resonances, the incident light couples strongly in the nanoparticle (Supporting Information Figure 2Sb−d). Therefore, since the SHG of the $BaTiO_3$ nanoparticles originates from the bulk,[31] an enhanced SHG is expected to occur when the electromagnetic field is strongly confined in the nanoparticle, at the resonances of the linear scattering spectrum. The positions of the linear scattering peaks and the SHG peaks are summarized in Table 1. Indeed, an enhanced SHG signal is detected at the *mq*- and *md*-peaks (peaks 1 and 3 in Figure 4a−d and column peak 1 and peak 3 in Table 1). In addition, an extra peak appears between the *mq*- and the *md*-peaks for all particles (peak 2 in Figure 4a−d and column peak 2 in Table 1). Comparing the position of this additional peak with the analytical Mie calculations (Figure 2h), we refer its origin to SHG enhancement at the *ed*-resonance of the scattering spectrum. The *ed*-resonance has its maximum between the *mq*- and the *md*-peaks (Figure 2h), similar to the additional peak in the SHG spectrum.

The enhancement of the SHG signal at the Mie resonances is not uniform. The possible origin of the nonuniformity of the SHG enhancement lies in the dependence of the SHG on the crystallographic structure. Indeed, the linear scattering cross-section is determined by the refractive index and the shape of the nanoparticle. However, in the case of the SHG, the crystal structure of the nanoparticle plays a crucial role. Therefore, the SHG enhancement depends not only on the position of the resonances in the scattering cross-section but also on the inner structure of the nanoparticle. The SHG is maximal if the crystallographic *c*-axis of the nanocrystal is parallel to the polarization of the incident beam. Figure 6Sa (Supporting Information) shows the dependence of the SHG on the polarization of the incident beam for the nanoparticle in Figure 4c,d. The orientation of the *c*-axis of the nanoparticle can be deduced from this measurement. Assuming the nanoparticle is monocrystalline, the quadrupole (butterfly) shape of the data indicates that the *c*-axis has an oblique angle with respect to the substrate. As a consequence, the SHG is not maximal, since the electric field is polarized in the plane parallel to the substrate. Additionally, the detailed crystal structure of the nanoparticle is not fully known, and it is possible that the nanoparticle is not perfectly monocrystalline or that the shell of the nanoparticle has a different crystal structure.[39,40] These factors could influence the SHG intensity. Lastly, the laser beam is focused on the nanoparticle through a 50× objective, and, as a consequence, the excitation beam can contain additional polarization components that further influence the intensity of the SHG due to the tight focusing configuration. Nevertheless, the measured SHG enhancement occurs at different wavelengths for each particle, and it clearly corresponds to the linear Mie resonances (Table 1). As a consequence, neither the crystal orientation nor the dispersion of the $\chi^{(2)}$ vector with the wavelength can be the only cause of such a strong dependence of the SHG signal on the incident beam wavelength. Further investigations are necessary to find out why the SHG enhancement has different intensities for each resonance and why the SHG peaks are slightly shifted with respect to the peaks in the linear spectrum. Simulations of the SHG emission intensity taking the crystal structure and shape of $BaTiO_3$ nanoparticles into account are currently in progress.

Influence of the Nanoparticle Shape, the Substrate, Collection Angle, and Incidence Angle on the Linear Cross-Section. The SHG signal is enhanced at the linear Mie resonances of single nanoparticles. Therefore, it is important to understand which factors influence the position and the shape of the linear resonant peaks, since the changes in the linear spectrum are affecting the nonlinear spectrum as well. The

DOI: 10.1021/acsphotonics.6b00570
ACS Photonics 2017, 4, 76−84

measured linear spectra of single particles (Figure 2a–g) show differences with respect to the linear spectra calculated with the Mie theory (Figure 2h). It has been reported that various factors such as the shape of the nanoparticle, the presence of the substrate, and the incidence angle affect the single-particle scattering spectrum.[5,41] To understand the influence of the nanoparticle shape, the glass substrate, and the collection angle, FEM simulations are performed in a commercial software (Comsol Multiphysics 5.2). In Figure 5 we compare the simulation with two measured linear spectra. Detailed results of the FEM simulations are presented in the Supporting Information and summarized here below.

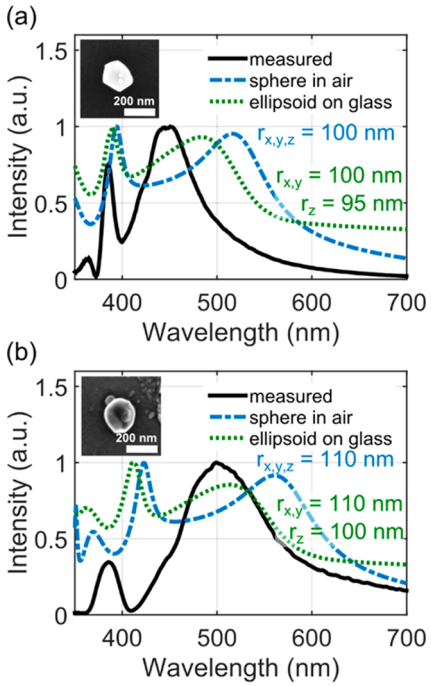

Figure 5. Comparison between the measured single-particle linear spectrum (solid line) and the results of the simulations (broken lines): The position of the peaks in the FEM simulation shifts closer to the position of the peaks in the measured linear spectrum when the glass substrate, ellipsoidal shape, and angle of incidence are also accounted for (green dotted line). The nanoparticle dimensions used in the simulation were chosen according to the SEM and AFM measurements. Insets: SEM micrographs of the measured nanoparticles.

Shape and Substrate. The AFM (Supporting Information Figure 7S) and SEM (Figure 2a–g, insets) measurements of the $BaTiO_3$ nanoparticles studied in this work show that their shape can be approximated to oblate ellipsoids. Therefore, we first study the influence of the nanoparticle shape on the scattering cross-section. We consider an ellipsoidal nanoparticles with semiaxis $r_x = r_y$ and $r_z \leq r_x$ in air or on a glass substrate (Supporting Information Figure 8Sa and b). This simulation shows that, when r_z decreases, both *mq*- and *md*-resonances blue-shift and the distance between the peaks decreases. In the presence of the glass substrate, the shape of the nanoparticle has a stronger influence on the behavior of the *mq*- and *md*-peaks. Thus, as the particle becomes more ellipsoidal in shape ($r_z < r_x$), both peaks are further blue-shifted and the *mq*-peak becomes significantly broader. Moreover, in the presence of the glass substrate, the ratio between the intensities of the *mq*- and the *md*-peaks starts to depend more on the shape of the nanoparticle. The *mq*-peak starts to dominate over the *md*-peak in the more ellipsoidal ($r_z < r_{x,y}$) nanoparticles, whereas the *md*-peak prevails over the *mq*-peak in the spherical ($r_z = r_{x,y}$) nanoparticles.

Collection Angle. The size of the $BaTiO_3$ nanoparticles used in this work are comparable to the wavelength of the incident light. Therefore, the nanoparticle do not emit in the Rayleigh regime, as electric dipoles. In the case of the measured nanoparticle, several other multipoles contribute to the linear response of the nanoparticles (Figure 2g). These multipoles do not emit isotopically in space (Supporting Information Figure 10S). Therefore, a detector with a limited aperture can collect only a fraction of the total linear response. We analyze the influence of the collection angle on the scattering cross-section of a single spherical nanoparticle (Supporting Information Figure 8Sc). We observe that the position of the *mq*-resonance remains almost unchanged as the collection angle decreases, whereas the *md*-resonance gets blue-shifted. The ratio between the intensities of the *mq*- and *md*-peak increases as the collection angle decreases.

Incidence Angle. In the dark field spectroscopy setup used in this work, the incident light has an oblique incidence (Figure 1 inset). Since the measured nanoparticles are ellipsoidal, the oblique incidence affects the position of the resonances. We study the influence of the incidence angle on an ellipsoidal nanoparticle with $r_{x,y}$ = 100 nm and r_z = 80 nm (Supporting Information Figure 8Sd). We observe that the position of the *md*-peak is not influenced by the angle of incidence. On the other side, the position of the *mq*-peak is red-shifted by 10 nm when the incidence angle exceeds 45°.

We compare the results of the simulations with the measured scattering spectra of single nanoparticles. For this purpose, we consider ellipsoidal nanoparticles on a glass substrate illuminated under an incidence angle of 45°. The results for two nanoparticles are shown in Figure 5. We observe that the scattering cross-sections calculated in the FEM simulations are in a better agreement with the measured scattering spectra than before accounting for the particle shape, the substrate, and the angle of incidence. Indeed, we showed that the ellipsoidal shape of a nanoparticle and the glass substrate cause a blue-shift of the center wavelengths of the resonances (Figure 5a,b). Furthermore, the distance between *mq*- and *md*-peaks decreases in the presence of the glass substrate, when the nanoparticle is more ellipsoid in shape ($r_z < r_{x,y}$), and when the angle of incidence is taken into account. On the other side, the ratio between the *mq*- and *md*-peaks from the calculated spectra is in disagreement with the measured ratio. In all the measured scattering spectra, the *mq*-peak has lower intensity then the *md*-peaks, as opposed to the calculated scattering spectra. This discrepancy could be caused by the fact that, in the FEM simulation, the $BaTiO_3$ is modeled as a lossless material. The absorption due to the presence of the band gap in $BaTiO_3$ is not considered. The band gap in bulk $BaTiO_3$ occurs at 385 nm,[42] around the wavelength where the *mq*-peak is located. The lower intensity of the *mq*-peak can therefore also be explained by the increased absorption around the band gap.

In future works, the influence of the irregular shape of the nanoparticles on the linear scattering spectrum will be studied. The above-discussed calculations show that the shape of the nanoparticle has the strongest impact on the scattering cross-section. Therefore, the irregular shapes of the presented nanoparticle could further influence the width, intensity, and position of the linear scattering cross-section.

DOI: 10.1021/acsphotonics.6b00570
ACS Photonics 2017, 4, 76–84

CONCLUSION

We have measured the linear scattering spectra of individual $BaTiO_3$ nanoparticles. Using the analytical Mie theory of spherical $BaTiO_3$ nanoparticles of similar size, we have unambiguously identified the two peaks in the spectrum as the magnetic quadrupole and the magnetic dipole resonances.

We have also performed a precise wavelength-dependent measurement of the SHG signal generated by the same nanoparticles. We have demonstrated a strong reshaping of the SHG signal around the resonances in the linear scattering cross-section. A maximum SHG enhancement of more than 4 orders of magnitude compared to the bulk $BaTiO_3$ crystal is measured for a 200 nm $BaTiO_3$ nanoparticle. The influence of the crystal structure and orientation on the SHG enhancement will be further analyzed in future works.

Furthermore, we have conducted FEM simulations to study the influence of the nanoparticle shape, the glass substrate, the collection angle, and the incidence angle on the $BaTiO_3$ single-particle scattering spectrum and discussed the shift of the measured peaks and their relative intensities.

To further understand the properties of $BaTiO_3$ nanoparticles, the influence of the irregular nanoparticle shape and the influence of the incident beam polarization will be studied in a future work. The properties of smaller $BaTiO_3$ nanoparticles with linear resonances in the UV range are also of interest for bioimaging and nanolithography applications and will also be studied.

Our work demonstrates the double function of $BaTiO_3$ nanoparticles as a linear material with strong electromagnetic responses and as a nonlinear material with strong SHG signals around the resonances of the linear spectrum. Furthermore, we have found indications that the electric dipole resonance, which is not visible in the linear spectrum, might be revealed in the nonlinear spectrum. We have proved that the size of the $BaTiO_3$ nanoparticles should be tailored according to the context where the nanoparticle is used. Even though $BaTiO_3$ nanoparticles were successfully used for in vivo imaging[43] and biolabeling,[30,44] these applications are affected by the weak SHG conversion efficiency, which limits the quality of the images and their interpretation. They also require high laser power, which can damage the biological sample. A highly sensitive interferometric setup can also be used to measure weak SHG signals.[45] However, simple and robust techniques with bright probes remain the preferred method for bioimaging. Our work can contribute to the improvement of these setups by demonstrating a strategy to obtain brighter probes with smaller sizes. Finally, we have extended the field of all-dielectric nanoparticles to second-order nonlinearities by using a perovskite non-centrosymmetric material that is transparent in a broad range of wavelengths, and we opened up new possibilities for enhancing low signals by taking advantage of the shape of individual nanoparticles specifically for biological applications.[43−45]

METHODS

Sample Preparation. The $BaTiO_3$ nanoparticles are provided in powder form by the group of Vincenzo Buscaglia from the Institute for Energetics and Interphases, National Research Council, Genoa, Italy. The powder is prepared by precipitation from an aqueous solution of metallic chlorides in strong alkaline conditions.[32] XRD measurements are performed on the $BaTiO_3$ powder, showing that more than 90% of the nanoparticle has a tetragonal crystal structure and less than 10% has a cubic crystal structure (Supporting Information Figure 1S). The $BaTiO_3$ nanoparticles have an ellipsoidal form with irregularities and polyhedral smooth facets (Figure 2a−g, insets).

A nanoparticle suspension of low concentration (0.05 μg/mL) is prepared and sonicated in order to obtain a uniform distribution of nanoparticles. The suspension is spin coated on a glass substrate covered with a 10 nm film of ITO. Prior to spin coating, the glass substrate is patterned with gold coordinates deposited by photolithography and lift off. Single particles with diameters of 200−250 nm are localized on the glass substrate by dark field microscopy and measured by scanning electron microscopy or atomic force microscopy.

Linear Scattering Measurement. The linear scattering spectra of single $BaTiO_3$ nanoparticles are measured in a dark field spectroscopy setup (Figure 1). The nanoparticle is positioned on the stage of a microscope (Zeiss Axio Imager Am1), and the light of a halogen lamp is focused on the sample with a 50× objective (Zeiss LD EC Epiplan Neofluar). The scattered light is collected with the same objective and analyzed with a high-precision spectrometer (Acton SP-2356 from Princeton Instruments, equipped with a thermoelectrically cooled CCD camera, Pixis 256E). A CMOS color camera is connected to a second exit of the microscope to collect optical dark field images of the measured nanoparticles and ensure the alignment of the nanoparticle and the collection area of the optical fiber. The nanoparticle is aligned with the optical fiber using a manual $x-y$ stage. The optical fiber acts as a pinhole and collects the signal coming from an area with a diameter of 5 μm.

The incidence angle of the light has an average value of 44.5°. The objective has a numerical aperture of 0.55, resulting in a collection angle of the backscattered light of 66.8° (Figure 1 inset).

The background contribution to the scattered signal is subtracted, and the signal is normalized by the halogen lamp spectrum. The halogen lamp spectrum was detected in the same configuration using a 99% scattering surface.

Second-Harmonic Generation Spectrum Measurement. The SHG signal of single $BaTiO_3$ nanoparticles is detected in a commercial two-photon inverted microscope (Leica SP8, Supporting Information Figure 4S). This system is equipped with a fs laser (MaiTai XD from Spectra Physics). The laser beam is focused on the sample through a 20× objective (Leica HC Plan Apochromat) and scanned over an area of 144 μm^2 around the $BaTiO_3$ nanoparticle. The diffraction-limited laser beam spot size has a diameter between 800 nm and 1.1 μm. The scattered signal is collected through the same objective, and the laser beam is blocked by a combination of short-pass filters (SP680 ET from Chroma-Technology and SP500 with OD > 4 from EdmundOptics). The SHG signal is detected with a hybrid detector (GaAsP detector from Hamamatsu) for pump wavelengths between 710 and 950 nm. The raw data are normalized by the incident power at the sample position, the quantum efficiency of the hybrid detectors, and the transmission of the optics in the setup.

The SHG is also measured in a home-built microscope (Figure 3). A fs laser beam (MaiTai DeepSee from Spectra Physics) is focused on the nanoparticle through a 50× objective (Zeiss LD EC Epiplan Neofluoar). The laser beam spot has an area of 1 to 2 μm. The SHG signal is collected with the same

DOI: 10.1021/acsphotonics.6b00570
ACS Photonics 2017, 4, 76−84

objective and measured with a high precision spectrometer (Acton SP-2356 from Princeton Instrument, equipped with a thermoelectrically cooled CCD camera, Pixis 256E). An EMCCD camera is used to ensure the alignment of the laser beam and the measured particle. Additional color filters (BG39 from Schott) were placed in the front of the spectrometer and camera to filter the residual laser beam. The SHG intensity is measured with the spectrometer. The spectrum for each laser wavelength is fitted to a Gaussian. The area of the Gaussian is proportional to the SHG signal. The raw data are normalized by the incident laser power, the sensitivity of the spectrometer, and the transmission/reflection of the optical components in the setup.

The SHG depends strongly on the polarization of the incident laser beam. The strongest SHG signal is obtained when the crystallographic *c*-axis of the nanocrystal is parallel to the incident field. The SHG spectrum was measured for the incident field polarization rendering the strongest SHG signal.

Analytical and Numerical Simulations. The scattering cross-section of individual $BaTiO_3$ nanoparticles is calculated according to the Mie theory using Matlab.[46] The algorithm assumes that a spherical $BaTiO_3$ nanoparticle is excited under normal incidence in a homogeneous medium (air). The total scattering cross-section over a solid angle of 4π was calculated. The refractive index values of $BaTiO_3$ were taken from the literature[33] (n_{BaTiO3} = 2.4953 for λ = 500 nm). The refractive index of air was approximated to the value for a vacuum (n_{air} = 1).

To account for the nanoparticle shape, the substrate, the collection angle, and the incidence angle, additional simulations are performed using a FEM commercial software (Comsol Multiphysics 5.2). The refractive index of glass is taken from the literature.[47] Two nanoparticle shapes are analyzed: perfectly spherical and ellipsoid with two equal semiaxes. The glass substrate is modeled as a semi-infinite medium. The nanoparticle is placed in air, in close proximity to the interface between air and glass. The incident field propagates perpendicular to the air−glass interface and has a linear polarization. The Fresnel coefficients are used to define the background field in glass and in air. The scattering cross-section is determined by integrating the Poynting vector over a surface.

■ ASSOCIATED CONTENT

Supporting Information

The Supporting Information is available free of charge on the ACS Publications website at DOI: 10.1021/acsphotonics.6b00570.

Nanoparticle characterization; detailed discussion of the simulations of the scattering cross-section of single $BaTiO_3$ nanoparticles; polar response of the SHG signal of single $BaTiO_3$ nanoparticles and $BaTiO_3$ bulk crystal; spectral analysis of the SHG (PDF)

■ AUTHOR INFORMATION

Corresponding Author

*E-mail: ftimpu@phys.ethz.ch.

ORCID

Flavia Timpu: 0000-0002-0951-4070

Notes

The authors declare no competing financial interest.

■ ACKNOWLEDGMENTS

The authors want to thank Dragomir Neshev and Mihail Petrov for helpful discussions, Teresa and Vincenzo Buscaglia for synthesizing and providing the $BaTiO_3$ nanoparticles, and Michal Wojdyr for preliminary measurements. Furthermore, the authors acknowledge support of the Scientific Center for Optical and Electron Microscopy (ScopeM) of the Swiss Federal Institute of Technology (ETHZ). Finally, the authors acknowledge the Swiss National Science Foundation grant 150609 for financial support.

■ REFERENCES

(1) Zhao, Q.; Zhou, J.; Zhang, F.; Lippens, D. Mie Resonance-Based Dielectric Metamaterials. *Mater. Today* **2009**, *12* (12), 60−69.

(2) Jahani, S.; Jacob, Z. All-Dielectric Metamaterials. *Nat. Nanotechnol.* **2016**, *11* (1), 23−36.

(3) Polman, A.; Atwater, H. A. Plasmonics: Optics at the Nanoscale. *Mater. Today* **2005**, *8* (1), 56.

(4) Bohren, C. F.; Huffman, D. R. *Absorption and Scattering of Light by Small Particles*; John Wiley & Sons, 2008.

(5) Fu, Y. H.; Kuznetsov, A. I.; Miroshnichenko, A. E.; Yu, Y. F.; Luk'yanchuk, B. Directional Visible Light Scattering by Silicon Nanoparticles. *Nat. Commun.* **2013**, *4*, 1527.

(6) García-Etxarri, A.; Gómez-Medina, R.; Froufe-Pérez, L. S.; López, C.; Chantada, L.; Scheffold, F.; Aizpurua, J.; Nieto-Vesperinas, M.; Sáenz, J. J. Strong Magnetic Response of Submicron Silicon Particles in the Infrared. *Opt. Express* **2011**, *19* (6), 4815−4826.

(7) Krasnok, A. E.; Simovski, C. R.; Belov, P. a; Kivshar, Y. S. Superdirective Dielectric Nanoantennas. *Nanoscale* **2014**, *6* (13), 7354−7361.

(8) Kuznetsov, A. I.; Miroshnichenko, A. E.; Fu, Y. H.; Zhang, J.; Luk'yanchuk, B. Magnetic Light. *Sci. Rep.* **2012**, *2*, 492.

(9) Evlyukhin, A. B.; Eriksen, R. L.; Cheng, W.; Beermann, J.; Reinhardt, C.; Petrov, A.; Prorok, S.; Eich, M.; Chichkov, B. N.; Bozhevolnyi, S. I. Optical Spectroscopy of Single Si Nanocylinders with Magnetic and Electric Resonances. *Sci. Rep.* **2014**, *4*, 4126.

(10) Liu, W. Ultra-Directional Super-Scattering of Homogenous Spherical Particles with Radial Anisotropy. *Opt. Express* **2015**, *23* (11), 14734−14743.

(11) Boyd, R. W. *Nonlinear Optics*; Academic Press, 2003.

(12) Kauranen, M.; Zayats, A. V. Nonlinear Plasmonics. *Nat. Photonics* **2012**, *6* (11), 737−748.

(13) Canfield, B. K.; Husu, H.; Laukkanen, J.; Bai, B.; Kuittinen, M.; Turunen, J.; Kauranen, M. Local Field Asymmetry Drives Second-Harmonic Generation in Noncentrosymmetric Nanodimers. *Nano Lett.* **2007**, *7* (5), 1251−1255.

(14) Butet, J.; Brevet, P. F.; Martin, O. J. F. Optical Second Harmonic Generation in Plasmonic Nanostructures: From Fundamental Principles to Advanced Applications. *ACS Nano* **2015**, *9* (11), 10545−10562.

(15) Bouhelier, A.; Beversluis, M.; Hartschuh, A.; Novotny, L. Near-Field Second-Harmonic Generation Induced by Local Field Enhancement. *Phys. Rev. Lett.* **2003**, *90* (1), 13903.

(16) Pu, Y.; Grange, R.; Hsieh, C.-L.; Psaltis, D. Nonlinear Optical Properties of Core-Shell Nanocavities for Enhanced Second-Harmonic Generation. *Phys. Rev. Lett.* **2010**, *104* (20), 207402.

(17) Richter, J.; Zilk, M.; Sergeyev, A.; Pertsch, T.; Grange, R. Core − Shell Potassium Niobate Nanowires for Enhanced Nonlinear Optical Effects. *Nanoscale* **2014**, *6* (10), 5200−5207.

(18) Lehr, D.; Reinhold, J.; Thiele, I.; Hartung, H.; Dietrich, K.; Menzel, C.; Pertsch, T.; Kley, E. B.; Tünnermann, A. Enhancing Second Harmonic Generation in Gold Nanoring Resonators Filled with Lithium Niobate. *Nano Lett.* **2015**, *15* (2), 1025−1030.

(19) Chen, P.-Y.; Argyropoulos, C.; D'Aguanno, G.; Alu, A. Enhanced Second-Harmonic Generation by Metasurface Nanomixer and Nanocavity. *ACS Photonics* **2015**, *2* (8), 1000−1006.

DOI: 10.1021/acsphotonics.6b00570
ACS Photonics 2017, 4, 76−84

(20) Linnenbank, H.; Grynko, Y.; Förstner, J.; Linden, S. Second Harmonic Generation Spectroscopy on Hybrid Plasmonic/Dielectric Nanoantennas. *Light: Sci. Appl.* **2016**, *5*, e16013.
(21) Casadei, A.; Pecora, E. F.; Trevino, J.; Forestiere, C.; Rüffer, D.; Russo-Averchi, E.; Matteini, F.; Tutuncuoglu, G.; Heiss, M.; Fontcuberta I Morral, A.; Dal Negro, L. Photonic-Plasmonic Coupling of GaAs Single Nanowires to Optical Nanoantennas. *Nano Lett.* **2014**, *14* (5), 2271−2278.
(22) Yang, Y.; Wang, W.; Boulesbaa, A.; Kravchenko, I. I.; Briggs, D. P.; Puretzky, A.; Geohegan, D.; Valentine, J. Nonlinear Fano-Resonant Dielectric Metasurfaces. *Nano Lett.* **2015**, *15* (11), 7388−7393.
(23) Shcherbakov, M. R.; Neshev, D. N.; Hopkins, B.; Shorokhov, A. S.; Staude, I.; Melik-Gaykazyan, E. V.; Decker, M.; Ezhov, A. A.; Miroshnichenko, A. E.; Brener, I.; Fedyanin, A. A.; Kivshar, Y. S. Enhanced Third-Harmonic Generation in Silicon Nanoparticles Driven by Magnetic Response. *Nano Lett.* **2014**, *14* (11), 6488−6492.
(24) Liu, S.; Saravi, S.; Keeler, G. A.; Sinclair, M. B.; Yang, Y.; Reno, J.; Pertsch, T.; Brener, I. Resonantly Enhanced Second-Harmonic Generation Using III-V Semiconductor All-Dielectric Metasurfaces. *Nano Lett.* **2016**, *16* (9), 5426−5432.
(25) Gili, V. F.; Carletti, L.; Locatelli, A.; Rocco, D.; Finazzi, M.; Ghirardini, L.; Favero, I.; Gomez, C. Monolithic AlGaAs Second-Harmonic Nanoantennas. *Opt. Express* **2016**, *24* (14), 6488−6492.
(26) Jellison, G. E. Optical Functions of Silicon Determined by Two-Channel Polarization Modulation Ellipsometry. *Opt. Mater. (Amsterdam, Neth.)* **1992**, *1* (1), 41−47.
(27) Jellison, G. E. Optical Functions of GaAs, GaP, and Ge Determined by Two-Channel Polarization Modulation Ellipsometry. *Opt. Mater. (Amsterdam, Neth.)* **1992**, *1* (3), 151−160.
(28) Webb, D. R.; Sipes, I. G.; Carter, D. E. In Vitro Solubility and in Viva Toxicity of Gallium Arsenide. *Toxicol. Appl. Pharmacol.* **1984**, *76* (1), 96−104.
(29) Wong, C.; Teng, Y. Y.; Ashok, J.; Varaprasad, P. L. H. Barium Titanate ($BaTiO_3$). *Handb. Opt. Constants Solids II* **1991**, 789−803.
(30) Staedler, D.; Magouroux, T.; Hadji, R.; Joulaud, C.; Extermann, J.; Schwung, S.; Passemard, S.; et al. Harmonic Nanocrystals for Biolabeling: A Survey of Optical Properties and Biocompatability. *ACS Nano* **2012**, *6* (3), 2542−2549.
(31) Kim, E.; Steinbrück, A.; Buscaglia, M. T.; Buscaglia, V.; Pertsch, T.; Grange, R. Second-Harmonic Generation of Single $BaTiO_3$ Nanoparticles down to 22 nm Diameter. *ACS Nano* **2013**, *7* (6), 5343−5349.
(32) Testinon, A.; Buscaglia, M. T.; Viviani, M.; Buscaglia, V.; Nanni, P. Synthesis of $BaTiO_3$ Particles with Tailored Size by Precipitation from Aqueous Solutions. *J. Am. Ceram. Soc.* **2004**, *87* (1), 79−83.
(33) Wemple, S. H.; Didomenico, M.; Camlibel, I. Dielectric and Optical Properties of Melt-Grown $BaTiO_3$. *J. Phys. Chem. Solids* **1968**, *29* (10), 1797−1803.
(34) de Beer, A. G. F.; Roke, S.; Dadap, J. I. Theory of Optical Second-Harmonic and Sum-Frequency Scattering from Arbitrarily Shaped Particles. *J. Opt. Soc. Am. B* **2011**, *28* (6), 1374−1384.
(35) Knight, M. W.; Wu, Y.; Lassiter, J. B.; Nordlander, P.; Halas, N. J. Substrates Matter: Influence of an Adjacent Dielectric on an Individual Plasmonic Nanoparticle. *Nano Lett.* **2009**, *9* (5), 2188−2192.
(36) Sergeyev, A.; Geiss, R.; Solntsev, A. S.; Sukhorukov, A. A.; Schrempel, F.; Pertsch, T.; Grange, R. Enhancing Waveguided Second-Harmonic in Lithium Niobate Nanowires. *ACS Photonics* **2015**, *2* (6), 687−691.
(37) Eltes, F.; Caimi, D.; Fallegger, F.; Sousa, M.; O'Connor, E.; Rossell, M. D.; Offrein, B.; Fompeyrine, J.; Abel, S. Low-Loss $BaTiO_3$ - Si Waveguides for Nonlinear Integrated Photonics. *ACS Photonics* **2016**, *3* (9), 1698−1703.
(38) Lin, P. T.; Wessels, B. W.; Jang, J. I.; Ketterson, J. B. Highly Efficient Broadband Second Harmonic Generation Using Polydomain Epitaxial Barium Titanate Thin Film Waveguides. *Appl. Phys. Lett.* **2008**, *92* (22), 90−93.
(39) Fang, C.; Zhou, D.; Gong, S. Core-Shell Structure and Size Effect in Barium Titanate Nanoparticle. *Phys. B* **2011**, *406* (6), 1317−1322.
(40) Hoshina, T.; Wada, S.; Kuroiwa, Y.; Tsurumi, T. Composite Structure and Size Effect of Barium Titanate Nanoparticles. *Appl. Phys. Lett.* **2008**, *93*, 192914.
(41) Zywietz, U.; Schmidt, M. K.; Evlyukhin, A. B.; Reinhardt, C.; Aizpurua, J.; Chichkov, B. N. Electromagnetic Resonances of Silicon Nanoparticle Dimers in the Visible. *ACS Photonics* **2015**, *2* (7), 913−920.
(42) Suzuki, K.; Kijima, K. Optical Band Gap of Barium Titanate Nanoparticles Prepared by RF-Plasma Chemical Vapor Deposition. *Jpn. J. Appl. Phys.* **2005**, *44* (4A), 2081−2082.
(43) Grange, R.; Lanvin, T.; Hsieh, C.-L.; Pu, Y.; Psaltis, D. Imaging with Second-Harmonic Radiation Probes in Living Tissue. *Biomed. Opt. Express* **2011**, *2* (9), 2532−2539.
(44) Hsieh, C. L.; Grange, R.; Pu, Y.; Psaltis, D. Bioconjugation of Barium Titanate Nanocrystals with Immunoglobulin G Antibody for Second Harmonic Radiation Imaging Probes. *Biomaterials* **2010**, *31* (8), 2272−2277.
(45) Macias-Romero, C.; Didier, M. E. P.; Zubkovs, V.; Delannoy, L.; Dutto, F.; Radenovic, A.; Roke, S. Probing Rotational and Translational Diffusion of Nanodoublers in Living Cells on Microsecond Time Scales. *Nano Lett.* **2014**, *14* (5), 2552−2557.
(46) Mätzler, C. *MATLAB Functions for Mie Scattering and Absorption*; Institute for Angew. Physics, No. 2002-08, Research Report.
(47) Malitson, I. H. Interspecimen Comparison of the Refractive Index of Fused Silica. *J. Opt. Soc. Am.* **1965**, *55* (10), 1205−1209.

DOI: 10.1021/acsphotonics.6b00570
ACS Photonics 2017, 4, 76−84